

Cavity-Enhanced Emission and Absorption of Color Centers in a Diamond Membrane With Selectable Strain

Robert Berghaus,¹ Selene Sachero,¹ Gregor Bayer,¹ Julia Heupel,² Tobias Herzig,³ Florian Feuchtmayr,¹ Jan Meijer,³ Cyril Popov,² and Alexander Kubanek^{1,*}

¹*Institute for Quantum Optics, Ulm University, Albert-Einstein-Allee 11, 89081 Ulm, Germany*

²*Institute of Nanostructure Technologies and Analytics,*

Center for Interdisciplinary Nanostructure Science and Technology,

University of Kassel, Heinrich-Plett-Str. 40, 34132 Kassel, Germany

³*Division of Applied Quantum Systems, Felix Bloch Institute for Solid State Physics,
University Leipzig, Linnestraße 5, 04103 Leipzig, Germany*

Group IV color centers in diamond are among the most promising optically active spin systems with strong optical transitions and long spin coherences. The ground-state splitting of the center is particularly important to suppress the interaction with coherence-limiting phonons, which improves the coherence properties and sets the upper limit for the operating temperature. Negatively charged silicon-vacancy centers have an ordinary ground-state splitting of only 48 GHz, resulting in required temperatures below one Kelvin, which can only be achieved by dilution refrigerators. Here, we increase the ground-state splitting by up to an order of magnitude by induced strain in a single-crystal diamond membrane. Furthermore, we demonstrate cavity-assisted spectroscopy enabled by coupling the emitter ensemble with a selectable strain to the mode of a Fabry-Perot microcavity. Calculation of the absorption cross-section yields $\sigma_{\text{abs}}^{\text{ens}} = 4.9 \cdot 10^{-11} \text{ cm}^2$. Together with the Purcell-enhanced twofold reduction in emitter lifetime below 1 ns, this makes the system a promising spin-photon interface at moderate temperatures of 4 K.

INTRODUCTION

Diamond, known as the hardest natural material, offers many outstanding properties not only for the classical world but also for fields such as quantum optics. A wide electronic band gap enables optical transparency and, at the same time, opens the possibility to host many different quantum emitters, known as color centers. In addition, the low concentration of intrinsic nuclear spins within the carbon lattice is an important prerequisite for isolating individual spins and avoiding unwanted interactions with the environment. Group IV color centers in diamond possess a strong optical transition with down to lifetime-limited linewidths at liquid helium temperatures. Their electron and nuclear spins are optically accessible, offering millisecond-long coherence times [1]. The electron spin coherence time is limited by a direct phonon process coupling both ground states [2]. Thus, a larger ground state splitting yields a longer electron spin coherence time [3, 4]. Group IV color centers in unstrained diamond crystal display an increasing ground-state splitting with increasing atomic number of the interstitial atom. Thus, those with higher atomic numbers are associated with longer electron-spin coherence times at moderate temperatures above 1 Kelvin. However, group IV centers with lighter atoms, such as the negatively-charged silicon-vacancy (SiV^-) center, can be engineered via strain to create a large ground-state splitting [5–7]. The effect of strain has been studied for different color centers in diamond.[8–10]. While strain control is a promising way

to improve the spin coherence properties, an efficient interface to photons is required to establish a spin-photon interface. Therefore, the coupling of the optical transition of the color centers to a predefined optical mode can be optimized through integration into an optical cavity [11]. Fabry-Perot (FP) resonators benefit from their full tunability, which makes them versatile. For example, the mode's resonance frequency can be adjusted to the transition frequency of the color center, which can be highly shifted by strain. While the successful integration of diamond into FP resonators has been demonstrated in numerous experiments [12–21], cavity enhancement of group IV centers in FP resonators at cryogenic temperatures remains challenging. It yet has only been achieved in a small number of experiments as shown with the SiV^- center [22, 23] as well as with the negatively-charged germanium-vacancy (GeV^-) center [24] and tin-vacancy (SnV^-) center [25]. Diamond integration is achieved using either a smooth diamond membrane (DM) or a nanoparticle for low scattering losses and short cavity lengths.

Here, we couple a DM with implanted SiV^- color centers under strain to the mode of an open-access FP microcavity. We fabricated the single-crystal DM with ensembles of SiV^- centers and show how different strain regions shift the SiV^- optical transitions allowing for increased ground-state splitting as exploited in GeV^- and SnV^- . This allows for the selective use of emitters with a different and intrinsic strain environment. By integrating the DM with negligible scattering losses into our tunable FP cavity, we reach finesse values of up to 2800 and address the ensemble with cavity-assisted photoluminescence (PL) and photoluminescence excitation (PLE). We enhance the optical C-transition of the SiV^- centers with the cavity-emitter system due to the twofold Purcell

* Corresponding author; alexander.kubanek@uni-ulm.de

effect and establish absorption spectroscopy within our cavity, where we measure an absorption cross-section of the emitter ensemble of up to $\sigma_{\text{abs,ens}} = 4.9 \cdot 10^{-11} \text{ cm}^2$.

METHODS

Single-Crystal Diamond Membrane

The single-crystal DM was fabricated by inductively coupled plasma reactive ion etching (ICP-RIE; PlasmaLab 100, Oxford Instruments plc), according to reference [26]. Prior to structuring, the electronic grade single-crystal diamond ($20 \mu\text{m} \times 2 \text{ mm} \times 2 \text{ mm}$; Applied Diamonds Inc.) was cleaned with piranha solution (3:1, 1 h) and treated in an oxygen plasma asher (150 W, 0.7 mbar, 2 min; TePla 200-G, PVA TePla AG). To withstand the long etching processes and to create a thinned diamond area of $1 \text{ mm} \times 1 \text{ mm}$, a rectangular bulk diamond mask (Medidia GmbH) was utilized. The mask provides an angled inlet to prevent over-etching towards the membrane edges. Using an Ar/Cl₂ + O₂ cyclic recipe, the diamond area was thinned to a minimum thickness of 850 nm, see Appendix A. The Ar/Cl₂ steps provide a smoothing effect, while the O₂ steps have a high etch rate to etch deep into the diamond.

Creation of Color Centers

A dense SiV⁻ ensemble (fluence of $3 \cdot 10^{11}$ per cm²) created by high dose implantation of ²⁸Si at 72 keV resulted in a mean implantation depth of 50 nm. 95 % of the ions reached a depth within the DM between 25 nm and 75 nm, see Appendix B. Implantation was followed by high-temperature annealing [27], for 1 h at 1200°C and 1500°C and cleansing with hydrofluoric acid and tri-acid. From the fluence and an expected emitter creation yield of 5 % per silicon ion we estimated an emitter density of $1.5 \cdot 10^{10}$ per cm².

Experimental Platform

Fig. 1(a) displays the implanted single-crystal DM bonded to a flat distributed Bragg reflector (DBR) for later cavity integration. For a <100> diamond facet, the projected dipoles of four possible SiV⁻ orientations within the D_{3d} symmetry form two orthogonal classes [5]. The two classes are sketched with the red marked silicon atoms surrounded by carbon atoms overlaid with the microscope image. This results in a perpendicular dipole emission for all four possible transitions between the two emitter classes. For cavity integration, a smooth diamond surface is necessary to minimize scattering losses. Additionally, the even surface enables strong bonding to the mirror via van der Waals forces [26]. An atomic force microscopy scan (Fig. 1(b)) of the DM surface reveals a

planar surface with a root mean square roughness of less than 0.5 nm within the scan area. The confocal and cavity mode areas are shown for comparison. Resulting scattering losses below 160 ppm allow finesse values \mathcal{F} above 40000.

Fig. 1(c) depicts the optical confocal setup, with the flexibility to include the curved cavity mirror for cavity assembly within the same setup. Whether free space or cavity experiments were conducted within the liquid helium bath cryostat (Oxford Instruments plc), the setup was cooled indirectly by a liquid nitrogen shield, or immersed in liquid helium for low temperatures and narrow optical transitions. The hemispherical cavity was formed by a macroscopic flat mirror and a curved mirror, structured by CO₂-laser ablation. For 737 nm, the transmission of the DBR coatings was designed and measured as $T = 1000$ ppm, allowing for a finesse of up to $\mathcal{F}_{\text{theo}} = 3140$, with a stopband between 610 nm and 750 nm. For longer wavelengths, the transmission then increased to around $T \approx 1\%$ at 788 nm. The plane cavity mirror was placed on nanopositioners (ANPx101 and ANPz101, attocube systems AG) to scan the DM and for cavity length tunability. For excitation and detection an aspherical lens ($f = 8 \text{ mm}$, NA = 0.55; AHL10-08-P-U, asphericon GmbH) focused into the diamond in confocal mode or coupled the optical microcavity when the upper curved mirror was placed inside the cryostat, see Appendix C for more details.

Temperature-dependent spectra of the SiV⁻ ensemble are shown in Fig. 1(d). The double peak, most prominent at 5 K, originates from the two emitter classes. Strain shifts the transitions in the spectral domain due to different transverse and longitudinal strain components on the emitters. While the transverse strain affects the ground-state splitting, the longitudinal strain mainly shifts the entire zero phonon line (ZPL) spectrum. An increased ground-state splitting increases the upper limits for the spin coherence time T_2 , which is mainly limited by acoustic phonon processes [2]. The expected order of the coherence time, based on one phonon interaction [2], is shown in Fig. 1(e) depending on the orbital ground-state splitting Δ_{gs} and the operating temperature. Spin coherence control and a prolongation could be demonstrated for SiV⁻ centers in nano-electrical-mechanical systems with externally applied strain [5, 6].

RESULTS AND DISCUSSION

Spectroscopic analysis of the SiV⁻ emitter ensemble was performed at 4 K directly on the mirror in confocal mode. The region of interest is marked in the microscope image Fig. 2(a), which corresponds to the densely implanted part. Thickness variations become evident by following the interference fringes [28] from the thin (850 nm) middle part towards the thicker implanted region (up to $3 \mu\text{m}$). Under off-resonant excitation around 712 nm, photoluminescence of the ZPL was collected. While scan-

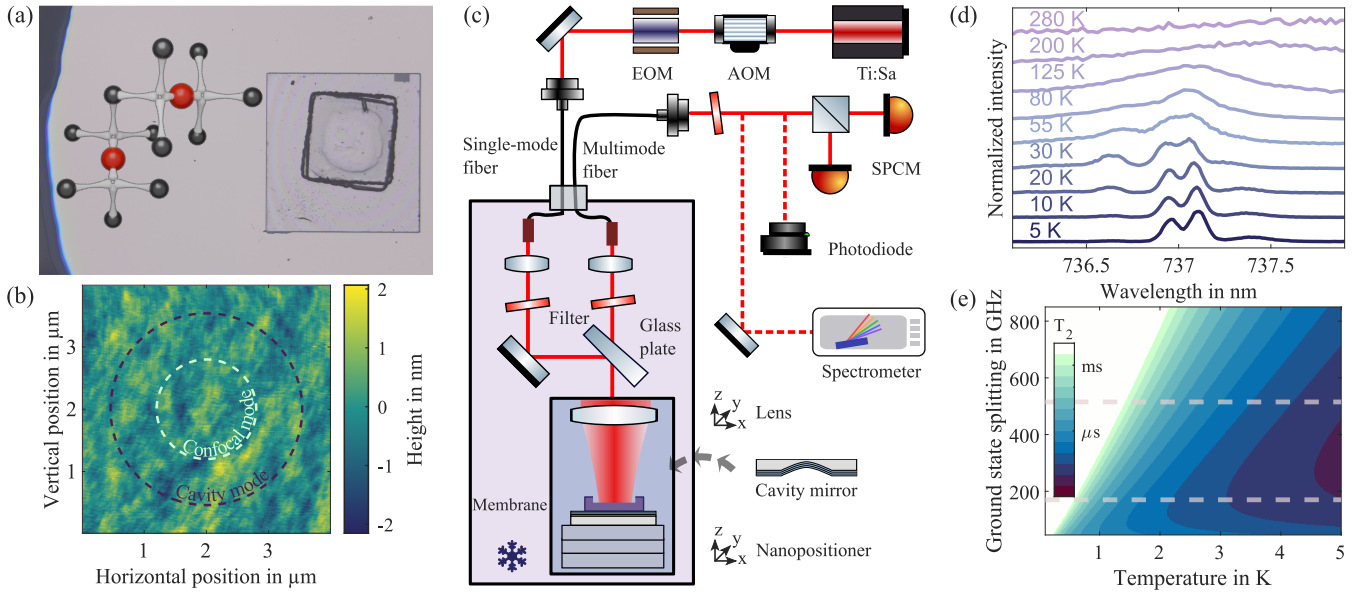


Fig. 1. **A strained single-crystal diamond membrane with implanted SiV⁻ centers for integration into an open-access microcavity.** (a) Microscope image of the thin diamond membrane bonded to the flat cavity mirror. The two overlapping rectangles indicate the etched inner part of the membrane. Inside: Sketch of the diamond lattice showing two different SiV⁻ centers. (b) Atomic force microscope image of the etched membrane after fabrication, representing a low surface roughness of below 0.5 nm, with the confocal and cavity mode areas indicated. (c) Sketch of the cryogenic experimental setup for confocal microscopy and cavity experiments, with the upper concave mirror mounted. The purple shaded area indicates the bath cryostat and the blue shaded area the confocal/cavity part. (d) Temperature-dependent photoluminescence spectra of the SiV⁻ emitter ensemble in confocal mode, indicating two classes of emitters. (e) Expected order of the coherence time T_2 as a function of different ground-state splittings Δ_{gs} and temperature due to phonon limitations.

ning the DM on the mirror horizontally and vertically the count rate within the implanted region was recorded (Fig. 2(b)). Fringes resulting from thickness variations follow a periodicity of $\lambda/(2n)$ [20], with $n = 2.4$ the refractive index of diamond.

Emitter Ensemble Strain Spectroscopy

Selected spectra from differently strained regions are shown in Fig. 2(c). The typical SiV⁻ ZPL emission (upper panel) at 737 nm with a four-line structure, labeled A to D, was observed for the ensemble. The ground-state splitting of $\Delta_{\text{gs}} = 170$ GHz is more than three times larger than the spin-orbit coupling of unstrained SiV⁻. The excited-state splitting with $\Delta_{\text{es}} = 380$ GHz shows an increase of 1.5. From the emitter density, we estimated an average number of $N \approx 85$ contributing emitters in the confocal mode $A = \frac{\pi}{4}\omega_{\text{fs}}^2$ with a beam waist of $\omega_{\text{fs}} \approx \frac{2\lambda}{\pi N A} \approx 0.8 \mu\text{m}$. Resonant excitation of strongly axially strained emitters with transition wavelengths above 738 nm, revealed single photon emission. See Appendix D for the first report of a single SiV⁻ inside a DM. For the two perpendicular emitter orientations, the strain environment shifts the transitions differently (Fig. 2(c), second and third panels). The most prominent C-line is therefore split. At a strong transverse strain of the order of $2 \cdot 10^{-4}$ with respect to [5],

the ground states split by 550 GHz, corresponding to almost 1 nm (Fig. 2(c), lower panel). This corresponds to an 11-fold increase in ground-state splitting compared to no strain.

We spectrally map the strain of the emitter ensemble over a wide range within the single-crystal membrane. Horizontal (H1, H2) and vertical line (V1, V2) scans with the changing ZPL emission are shown in Fig. 2(d). The two emitter classes experience strong strain-induced shifts. Both classes are affected in regions of high strain, indicated by large shifts in the different optical transitions. Some spectral lines originating from different emitter classes feature crossings of spectral lines. We attribute the strain to the bond, different thermal expansion coefficients of diamond and DBR, and the fabrication process. A comparable ground-state splitting of up to $\Delta_{\text{gs}} \approx 500$ GHz was shown in a nanophotonic crystal cavity with implanted SiV⁻ centers [8], where strain variations are attributed to the fabrication process. For the heavier group IV color centers including SnV⁻, strain can simplify spin control due to required orbital mixing in the spin ground states [9, 29, 30]. Hence, an intentional mismatch of the thermal expansion coefficients between a diamond membrane and the substrate rendered a tensile strain on SnV⁻ centers within the crystal in recent works [9, 10]. Work on FP cavity-enhanced GeV⁻ reported an increase of the ground-state splitting up to a factor of 7 [24]. While these works probe the strain at a few points,

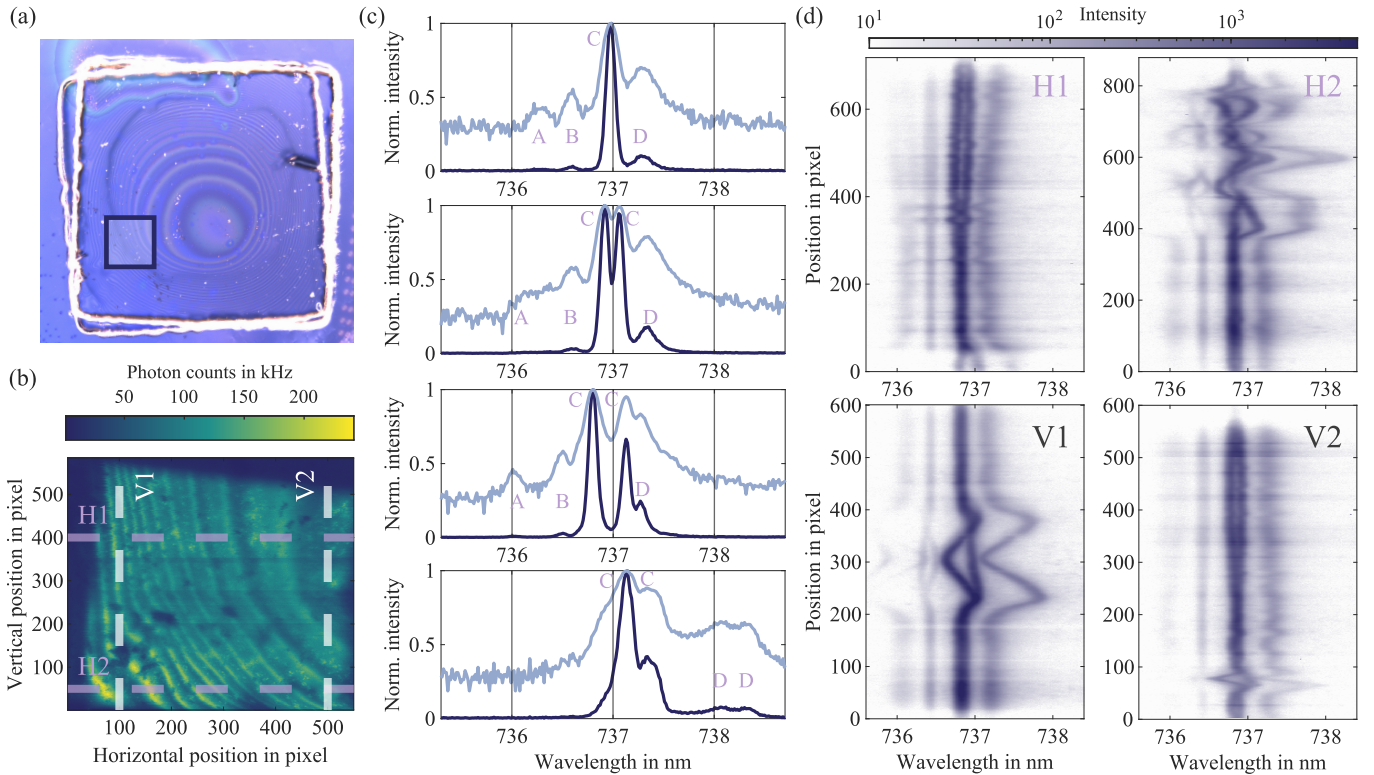


Fig. 2. **Strain-dependent zero phonon line emission of the SiV⁻ emitter ensemble at 4K.** (a) Differential interference contrast microscope image of the etched membrane. Fringes indicate height changes. The blue rectangle represents the implanted region. (b) Confocal membrane-on-mirror characterization of the implanted area under off-resonant excitation. Fringes result from decreasing thickness toward the upper right of the confocal scan. Dashed lines indicate line scans from the spectral analysis in (d). (c) Spectra (dark blue) showing different strain configurations. The spectra are also shown with a logarithmic scaling (light blue) for better visibility of the less prominent peaks. (d) Emission wavelengths of SiV⁻ emitters along horizontal and vertical lines depicted in confocal scan (a). A spectrum was recorded at each position of the line scan with scan directions from left to right and bottom to top. The two bright lines in each scan show the C-transition of two different SiV⁻ orientations. Spectral shifts are a result of non-uniform strain in the diamond crystal.

we show the strain profile over a wide range, especially up to a high-strain regime. Emitters with desired strain properties can be selected by adjusting the position of the membrane in the optical mode. In particular, these include emitters with a large ground-state splitting that possess superior coherence properties and promise operating temperatures above 1 K.

Cavity Integration

We closed the cavity by mounting a concave mirror with a radius of curvature (RoC) of 19.7 μm and an ellipticity of 0.19. This allowed cavity-assisted experiments within the same setup. The schematic in Fig. 3(a) depicts the mirror configuration and indicates the direction of the reflection and transmission signals from the microcavity. Often, FP microcavities are composed of a mirror-fiber combination [16, 31, 32] or even a fiber-fiber [33, 34] assembly. For an efficient and mode-matched operation, we used two mirrors on plain silica substrates and coupled free space into fiber optics [35]. The cavity length could

be controlled by tuning the piezo crystal voltage of the z nanopositioner. X and y nanopositioners allowed the positioning of the plane mirror, here such that the top right of the implanted region lay within the cavity mode.

Fig. 3(b) shows two typical cavity-length scans probing the resonance of a fundamental Gaussian mode on the diamond membrane. A laser applied to the cavity revealed the reflected and transmitted intensity, in this case at 80 K. The cavity length change was calculated by considering a length difference of 737/2 nm between the two resonances. Including the membrane, we experimentally observed a finesse of $\mathcal{F}_{\text{exp}} = 2800$ for air-like modes [36], close to the theoretical finesse. Within air-like modes, we conclude that scattering losses are negligible for one given wavelength. All cavity experiments were performed within the upper right region of Fig. 2(b), where the two orientations of SiV⁻ showed a slight separation in the C-transitions. There, by following the interference fringes, the membrane has an estimated thickness of 1.2 μm . Operating at an effective cavity length of $L_{\text{eff}} \approx 10 \mu\text{m}$ the resonator possesses a linewidth of $\kappa/2\pi = 5.4 \text{ GHz}$, much broader than the Fourier transform limit of a single SiV⁻.

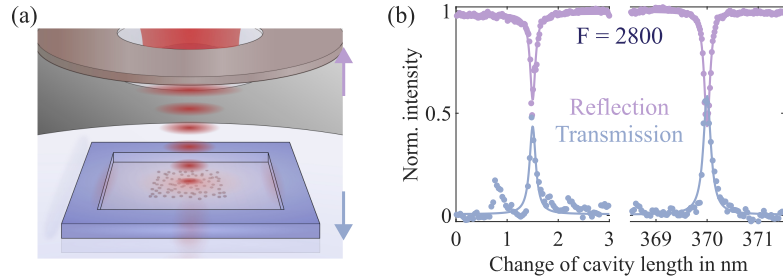


Fig. 3. **Cavity-integrated diamond membrane.** (a) Sketch of the membrane bonded to the flat mirror of the cavity, with the excitation laser coupled from above through the curved mirror. (b) Cavity length scans over two cavity resonances in reflection (purple) and transmission (blue) at 80 K. Data points as dots and Lorentzian fits as lines. The transmission signal was normalized to the reflection signal, without considering additional losses.

center. From Gaussian beam optics, we calculated a resonator beam waist of $\omega_0 = 1.52 \mu\text{m}$ and the fundamental cavity mode volume of $V = 45.2\lambda_{\text{las}}^3$ (Appendix C). Additionally, we determined the quality factor $Q = 76000$ from \mathcal{F}_{exp} , see Tab. I for more details. This allowed for the estimation of the theoretical Purcell factor

$$f_{\mathcal{P}} = \frac{3}{4\pi^2} \left(\frac{\lambda}{n} \right)^3 \frac{Q}{V} \quad (1)$$

which we estimated to $f_{\mathcal{P}} = 9.2$.

Cavity-Modulated Photoluminescence and Photoluminescence Excitation

Within the cavity, off-resonant excitation was performed with one fundamental transverse mode of the cavity tuned to resonance with the ZPL and the next higher mode to resonance with the excitation laser at a lower wavelength of about 712 nm. Cavity length-dependent detection of the SiV⁺ emitters' ZPL in Fig. 4(a) shows PL with a mode volume V between 45 and $53\lambda_{\text{las}}^3$ at 120 K. The highest count rate was observed when the resonator condition $L_{\text{eff}} = m\frac{\lambda}{2}$ is best fulfilled for the ZPL and the laser simultaneously, here with the laser at resonance $m=30$ and the detection through mode $m=29$. This translates to an effective cavity length of $L_{\text{eff}} = 10.7 \mu\text{m}$. Spectral probing of the ZPL emission at 70 K is shown in Fig. 4(b), where the cavity resonance is in tune with the excitation laser. Adding up the spectra, two peaks become visible. The first results from transitions originating from the upper excited state and the second from the lower excited state.

For a resonant PLE probing, we tuned the laser to the ZPL and detected the cavity-modulated phonon sideband. In a length scan, we collected fluorescence when the laser was in resonance with the cavity. This reveals three fundamental transverse modes, plus additional higher-order modes as shown in Fig. 4(c). With the laser in resonance with the cavity ($m=27$) and the emitters' ZPL, we acquired a spectrum shown in Fig. 4(d). The sideband couples to the next two cavity modes ($m=26, 25$). Emission in mode $m=25$ at 797 nm is still

apparent, even with the reflectivity of the mirrors decreasing drastically. Resonant PLE probing is shown in Fig. 4(e) for 120 K, 70 K and 4 K. For every excitation wavelength, the cavity length was scanned multiple times while collecting the laser signal and the fluorescence signal. We summed the fluorescence counts, around the cavity resonance for every scan and normalized the data. Comparing the temperature-dependent spectra from within the cavity to the free space PLE data, the inhomogeneous linewidth is broader. We attribute this to the cavity mode area being more than 3 times larger than the confocal area resulting in more contributing emitters and a broader spectral distribution. With the larger probe area, we collected the emission from more emitters, including a wider range of strain values, so the emitter ensemble is wider spectrally distributed. At 4 K the C-line shows an inhomogeneous linewidth of $\nu_{\text{inh}} = 65.7 \text{ GHz}$ (25.1 GHz) within the cavity (free space), a factor of 10 broader than the cavity linewidth $\kappa/2\pi$. PL plus off-resonant and resonant PLE are well-established techniques for confocal microscopy of color centers, which we implemented for the cavity system. To verify the number of contributing emitters, we compared free space PLE counts of the ensemble to those of the single emitter from Appendix D. The power-corrected count rates differed by a factor of 45, which also reflects the number of emitters within the confocal mode, consistent with the implantation parameters. For the larger cavity mode, we expect an order of up to 150 contributing emitters.

In-Cavity Absorption of Emitter Ensemble

Quantum communication protocols profit from a direct way of resonantly manipulating and reading quantum states. Reflection-based approaches in nanophotonic cavities presented the crucial probing of a system by resonant excitation and detection [8, 37–39]. When we resonantly probed the emitters' emission out of the cavity, we also collected and separated the reflected laser signal by optical filtering. This provided information on the cavity in-coupling and scattering within the resonator.

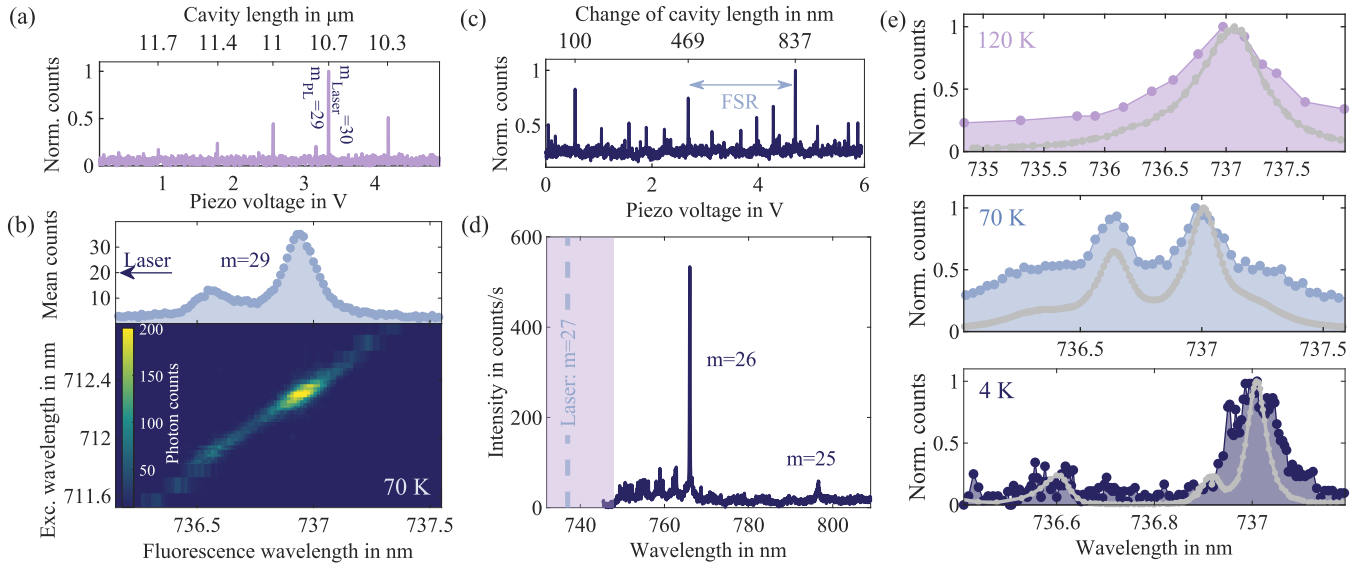


Fig. 4. **Cavity-assisted photoluminescence and photoluminescence excitation.** (a) Photoluminescence counts from cavity length scan under off-resonant excitation at 712.3 nm. (b) Spectra with cavity-modulated zero phonon line emission ($m=29$) under off-resonant excitation at 70 K. The excitation laser was resonant with the next higher cavity mode ($m=30$). The averaged counts from all spectra are shown at the top. (c) Cavity length scan under resonant excitation at 737 nm at 4 K. (d) Cavity-modulated sideband emission of the SiV^- emitters at a cavity length of 10 μm at 4 K. The excitation laser was resonant with the zero phonon line at 737 nm and the cavity mode $m=27$. (e) Temperature-dependent photoluminescence excitation, with a sideband collection. Free space data are shown in gray.

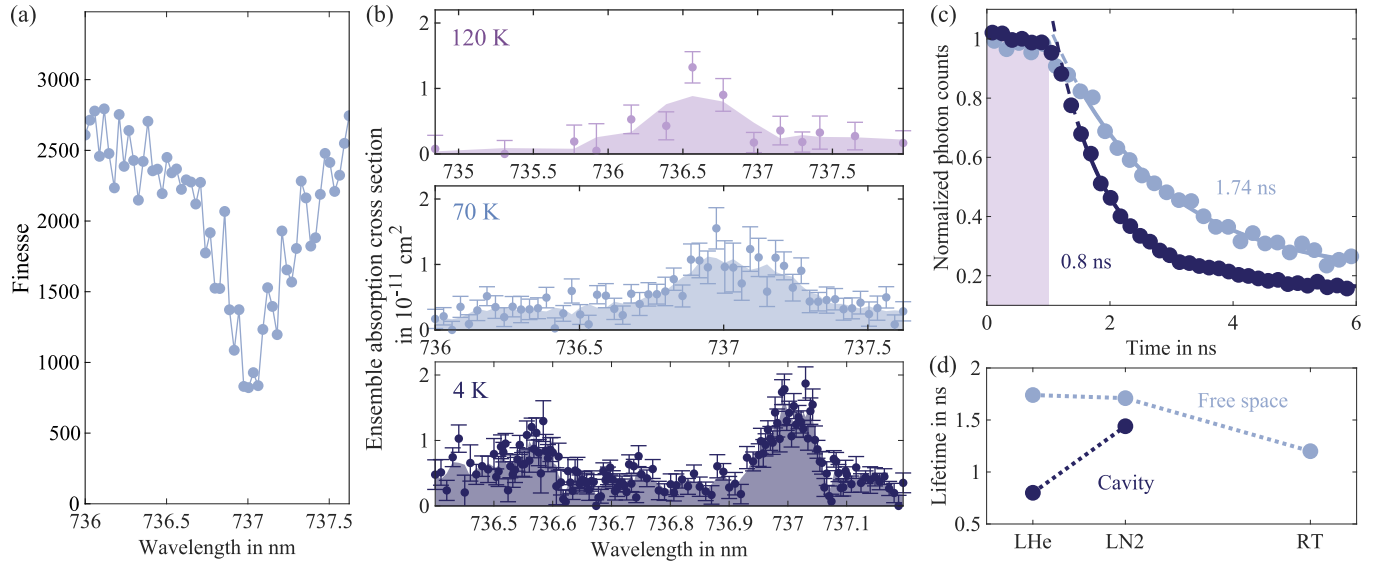


Fig. 5. **Absorption spectroscopy and Purcell enhancement of SiV^- transition.** (a) Highest observed finesse reduction due to absorption of the emitters. (b) Calculated absorption for the emitter ensemble for different temperatures. The cross-section (dots) was estimated from averaged finesse measurements. Error bars show the standard deviation, shaded area shows the moving average for better visibility. (c) Optical lifetime measurement of the C-transition without (light blue dots) and with the cavity (blue dots) with respective exponential decay (solid line) at 4 K. The purple area indicates the end of the laser pulse. (d) Optical lifetimes at different temperatures without (light blue dots) and with the cavity (blue dots). The dotted lines illustrate the trend.

We observed less prominent cavity resonances within an air-like mode when the system is resonant with the emitter ensemble. Probing the finesse, by scanning the cavity over two cavity resonances, showed reduced finesse values for the SiV^- wavelengths. Fig. 5(a) depicts such

measurement, with the highest observed finesse reduction at 70 K. The SiV^- ensemble inside the resonator absorbed the laser light, revealing the emitters' population. The emitter-cavity interaction directly imprints on the reflected laser signal. Absorption losses L_{SiV} introduced

Parameter	Condition	Symbol	Value	Unit	Origin
Membrane & emitter					
Minimal membrane thickness		l	850	nm	profilometer
Surface roughness		RMS	0.44	nm	atomic force microscope
Implantation depth		d	50	nm	implantation energy
Single emitter linewidth	4 K	ν_{single}	171.4	MHz	fitted PLE spectrum
Inhomogeneous emitter linewidth	4 K	ν_{inh}	25.1	GHz	fitted PLE spectrum
Mirror					
Radius of curvature x		RoC_x	17.6	μm	fitted interferometer data
Radius of curvature y		RoC_y	21.7	μm	fitted interferometer data
Mirror reflectivity	737 nm	R	99.9	%	reflection data from Laseroptik
Transmission	737 nm	T_{ppm}	1000	ppm	reflection data from Laseroptik
Cavity					
Theoretical finesse		$\mathcal{F}_{\text{theo}}$	3140		T_{ppm}
Experimental finesse		\mathcal{F}_{exp}	2800		cavity length scan
Typical cavity length		L_{eff}	10	μm	calculation from spectra
Typical cavity linewidth		κ	5.4	GHz	\mathcal{F}_{exp} and L_{eff}
Beam waist		ω_0	1.52	μm	L_{eff} and RoC
Typical mode volume		V	45.2	λ_{las}^3	ω_0
Typical mode number		m	27		calculation from spectra
Quality factor		Q	76000		\mathcal{F}_{exp} and m
Purcell enhancement					
Theoretical Purcell factor		$f_{\mathcal{P}}$	9.2		equation (1)
Cavity-emitter lifetime	70 K	τ_{cav}	1.44	ns	fitted lifetime data
Cavity-emitter lifetime	4 K	τ_{cav}	0.8	ns	fitted lifetime data
Effective Purcell factor	4 K	$F_{P,\text{eff}}$	2.2		equation (5)
Cooperativity	4 K	C	1.2		equation (7)

Tab. I. Membrane, emitter, and cavity parameters.

by the emitters can be calculated with [40]

$$L_{\text{SiV}} = \pi \left(\frac{1}{\mathcal{F}_{\text{SiV}}} - \frac{1}{\mathcal{F}_{\text{exp}}} \right). \quad (2)$$

\mathcal{F}_{exp} describes the finesse of the membrane-cavity system and \mathcal{F}_{SiV} the emitter-reduced finesse. Considering the maximum reduction of the finesse down to $\mathcal{F}_{\text{max}} \approx 820$ at the C-transition, the emitters together introduced losses of 2710 ppm. Combining the losses with the area of the resonator mode $A = 1.81 \mu\text{m}^2$ the absorption cross-section of the emitters can be obtained:

$$\sigma_{\text{abs}}^{\text{ens}} = L_{\text{SiV}} \cdot A. \quad (3)$$

We calculated an absorption cross section of $\sigma_{\text{abs}}^{\text{ens}} = 4.9 \cdot 10^{-11} \text{ cm}^2$ for the ensemble. For the number of contributing emitters N , the absorption cross-section of a single emitter excluding nonlinear effects [40] follows:

$$\sigma_{\text{abs}}^{\text{single}} = \frac{\sigma_{\text{abs}}^{\text{ens}}}{N}. \quad (4)$$

With approximately 150 emitters contributing, we calculated a cross-section of $\sigma_{\text{abs}}^{\text{single}} \approx 3.2 \cdot 10^{-13} \text{ cm}^2$ for a single emitter, which falls within the middle range of reported values [40, 41]. Furthermore, we calculated the absorption cross-section of the emitter-cavity system (Fig. 5(b)) from multiple cavity resonances for $T = (120, 70, 4)$ K, respectively. Comparing the highest ensemble absorption cross-section $\sigma_{\text{abs}}^{\text{ens}} = (1.3, 1.6, 1.9) \cdot$

10^{-11} cm^2 for these temperatures, the absorption enhances as the inhomogeneous linewidth of the emitters decreases with lower temperatures. Overall, absorption of the emitters can be determined due to good coupling of the emitter ensemble to the cavity mode. For a quantification of the enhancement, we performed ordinary lifetime measurements.

Purcell Enhancement

Experimental evidence for Purcell-enhanced lifetime-shortening is the direct comparison of the optical lifetime of the emitters in free space (τ_{fs}) with the lifetime inside the cavity field (τ_{cav}):

$$F_{P,\text{eff}} = \frac{\tau_{\text{fs}}}{\tau_{\text{cav}}} = 1 + \xi f_{\mathcal{P}}. \quad (5)$$

With the branching ratio ξ the theoretical Purcell factor from equation (1) can be connected with the effective Purcell factor $F_{P,\text{eff}}$. To determine the effective Purcell factor we measured the lifetime of the emitter ensemble at 4 K resonantly with the C-transition within the cavity and in free space under off-resonant excitation. The fitted lifetime data in Fig. 5(c) verify a shortening of the optical lifetime from $\tau_{\text{fs}} = 1.74 \text{ ns}$ to $\tau_{\text{cav}} = 0.8 \text{ ns}$. This results in a Purcell factor of $F_{P,\text{eff}} = 2.2$ at liquid helium temperatures (LHe). The free space lifetime is in good agreement with previous studies on the SiV⁻ color center

[2, 42, 43]. Under ambient conditions the free space lifetime was shorter, see Fig. 5(d). Again, this agrees with the studies and is attributed to the thermal activation of a non-radiative decay channel resulting in a poor quantum yield [42]. The measured free space optical lifetimes of the emitter ensemble and previous studies can be found in Tab. II in Appendix E. It follows that at liquid nitrogen temperature (LN2) the Purcell factor decreases ($F_{P,\text{eff}} = 1.2$), as the linewidth of the emitter ensemble broadens towards room temperature (RT), due to a reduced overlap of cavity and emitters' linewidth. The clear sign of the Purcell effect at 4 K, which enabled for higher emission rates of the strained emitters, allowed the estimation of important cavity parameters. These include the beta-factor

$$\beta = \frac{F_{P,\text{eff}} - 1}{F_{P,\text{eff}}}, \quad (6)$$

of $\beta = 0.54$ and the cooperativity

$$C = F_{P,\text{eff}} - 1 \quad (7)$$

of above 1, towards high cooperativity ($C \gg 1$).

CONCLUSION

In this work, we presented a diamond-cavity interface based on an ensemble of SiV^- centers coupled to the mode of an open Fabry-Perot resonator. The SiV^- ensemble created by ion implantation into a μm -thin diamond membrane possesses a wide range of laterally continuously varying strain values. The induced strain causes significant shifts of the fine-structure transitions, which differ for the different orientations of the SiV^- classes in the ensemble. The ground-state splitting Δ_{gs} reaches values of up to 550 GHz across the diamond membrane. The strain can be used to overlap the optical transitions of different classes of SiV^- centers, as observed by a crossing in the corresponding spectral lines. Furthermore, the large ground-state splitting is highly important for the future use of the system as a spin-photon interface at moderate temperatures above 1 Kelvin. Thus, a fully tunable microcavity enables to selectively choose specifically strained emitters. While lateral tunability allows the selection of an appropriate strain value, tunability of the resonance frequency enables deterministic coupling of individual transitions to the cavity mode. Cavity-assisted absorption yields a cross section of $\sigma_{\text{abs}}^{\text{ens}} = 4.9 \cdot 10^{-11} \text{ cm}^2$ of the SiV emitter ensemble resulting in $\sigma_{\text{abs}}^{\text{single}} \approx 3.2 \cdot 10^{-13} \text{ cm}^2$ for a single SiV^- color center. The lifetime shortening of the emitter ensemble in the sub-ns regime revealed a Purcell factor of $F_{P,\text{eff}} = 2.2$. The fourfold deviation from the theoretical predictions can be connected to the branching ratio. The resulting cooperativity of $C = 1.2$ yields the cavity quantum electrodynamics parameter set of $(g, \kappa, \gamma)/2\pi = (0.43, 5.4, 0.091)$ GHz.

FUNDING

The authors gratefully acknowledge the German Federal Ministry of Education and Research (BMBF) funding within the project QR.X (16KISQ005, 16KISQ006). The authors gratefully acknowledge the funding from the European Union and the DFG within the Quantera-project SensExtreme. S.S. acknowledges funding from the Marie Curie ITN project LasIonDef (GA n.956387).

ACKNOWLEDGMENTS

We thank Richard Waltrich and Susanne Menzel for their support in the cleaning process, Patrick Maier and Jan Schimmel for cavity structure fabrication, and Johannes Lang and Jens Fuhrmann for the annealing of the diamond sample. Most measurements were performed with the QuDi software suite [44].

DISCLOSURES

The authors declare no conflicts of interest.

DATA AVAILABILITY STATEMENT

Data underlying the results presented in this paper are not publicly available at this time but may be obtained from the authors upon reasonable request.

APPENDIX

A. Diamond Membrane Thickness

Scans taken with a profilometer (Dektak, Bruker Corp.) along the two axes of the DM show the thickness variations along the whole membrane, see Fig. 6. The minimum thickness in the two scans is 850 nm and 880 nm respectively, while the frame, used for handling the membrane, shows a thickness of 20 μm .

B. Implantation and Cleaning

An implantation depth inside the DM for the bonded side was calculated from Stopping Range of Ions in Matter (SRIM) simulation. Fig. 7 shows the simulated depth distribution of the ion concentration together with the estimated electric field inside the single crystal membrane. The electric field simulation for the diamond-mirror interface is based on a transfer-matrix, using the DBR coating design, and the assumption of the diamond bonded without an air gap. The highest ion concentration lies at 80% of the highest field intensity for 737 nm inside the

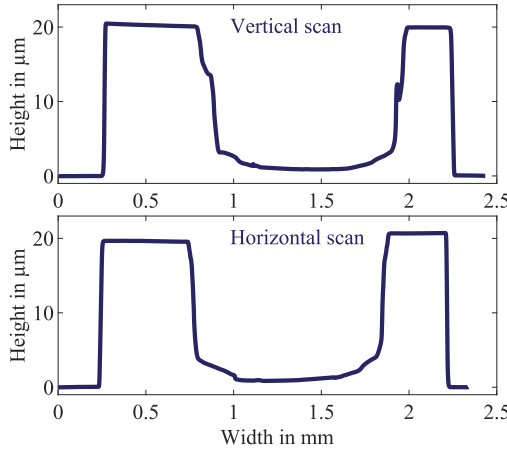


Fig. 6. **Height variation of the bonded diamond membrane along the main axes.** Horizontal (left to right) and vertical (bottom to top) scans with a profilometer, performed after all optical measurements, started and ended at the mirror surface. The dimensions of the diamond sample become apparent with the etched window of approximately 1 mm \times 1 mm.

diamond. The ion concentration allows for an estimation on the emitter creation yield. The creation of emitters in diamond by thermal annealing is generally of low efficiency [45]. Different values have been reported for the yield of SiV⁻, ranging from 2.5 % to 18 % [46–49].

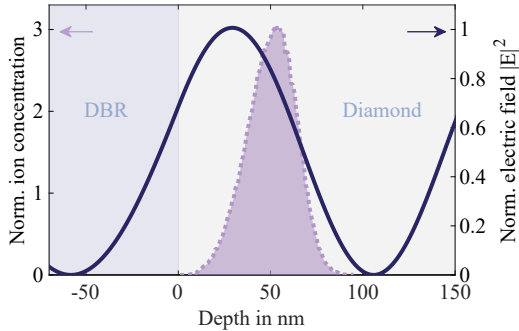


Fig. 7. **Diamond-mirror interface with electric field distribution and implantation depth inside the membrane.** The electric field (blue line) for 737 nm within the DBR (blue area) and the bonded membrane (gray area) from a transfer-matrix simulation, using the coating design, is shown. The implantation depth (purple, dashed line) from a SRIM simulation, indicates the overlap of the electric field with the emitters.

After implantation and annealing, the DM was cleaned and bonded three times. While the first bonding attempt with RT tri-acid cleaning resulted in reduced finesse values due to scattering losses, we performed a second attempt with standard tri-acid cleaning (130°C). This resulted in less loss, although still observable. The third approach involved hydrofluoric acid cleaning followed by tri-acid cleaning (130°C), which resulted in a strong bond

and negligible scattering losses within air-like modes. For bonding, the membrane was directly transferred from ultrapure water droplets onto the flat mirror.

C. Confocal Setup and Cavity Characteristics

For excitation, we used the laser light of an actively stabilized titanium-sapphire ring laser (Matisse 2 TS, Sirah Lasertechnik GmbH), power-stabilized with an acoustic optical modulator (AOM, 3350-199, Gooch & Housego Ltd.). For pulsed measurements, we employed a fiber-pigtailed amplitude electro-optical modulator (EOM, AM705, JENOPTIK AG) regulated by either a fast rise-time pulse generator (30 ps rise/fall time; LBE-1320, Leo Bodnar Electronics Ltd.) or an arbitrary waveform generator (AWG, M9502A, Keysight Technologies Inc.). The excitation laser was guided into the cryostat via a single-mode fiber (SM CU600PSC, IVG Fiber Ltd.) and then partially reflected by a wedge prism (0.5° Nom. 12.5 mm Dia. VIS-NIR, N-BK7 Wedge Prism, Edmund Optics) to the aspherical lens. For detection, the reflected laser and fluorescence signal out of the cavity was collected with a multimode fiber (MM FG050LGA, Thorlabs Inc.) and guided out of the cryostat. It was separated by spectral filtering: 730 notch filter (single notch filter 730 nm - zet 730NF, Chroma Technology Corp.), 740/13 bandpass filter (740/13 BrightLine HC, Semrock), 750 longpass filter (Thorlabs Inc. and AHF). The notch filter blocked the laser or unwanted fluorescence around the ZPL, the bandpass filtered the ZPL, and the longpass separated the laser signal from the phonon sideband. Laser light was sent to a silicon avalanche photodetector (APD120A2/M, Thorlabs Inc.), and fluorescence signal either to a single photon counting module (SPCMAQRH-14, Excelitas Technologies Corp.) or a spectrometer (SpectraPro HRS-500, Teledyne Princeton Instruments). Correlation measurements were conducted with a correlation device (Time Tagger Ultra module, Swabian Instruments GmbH). In transmission, the laser was directly detected with a silicon photodiode (S1337-66BQ, Hamamatsu Photonics K.K.) placed below the planar mirror.

Characterization of the spherical cavity structure (Fig. 8(a)) in a home-built Twyman-Green-interferometer revealed the RoC and the ellipticity, specified in the main text. Fig. 8(b) and 8(c) show the height profile from the interferometric analysis along the two vertical axes of the structure. For reference, spheres with the corresponding RoC from the fit are shown on top (dark blue). The RoC allowed for the calculation of the beam waist within the resonator

$$\omega_0 \approx \sqrt{\frac{\lambda}{\pi}} (L_{\text{eff}} R_{\text{OC}} - L_{\text{eff}}^2)^{1/4}, \quad (8)$$

used for the estimation of the fundamental cavity mode volume $V = \frac{\pi}{4} L_{\text{eff}} \omega_0^2$ and the cavity mode area $A = \frac{\pi \omega_0^2}{4}$.

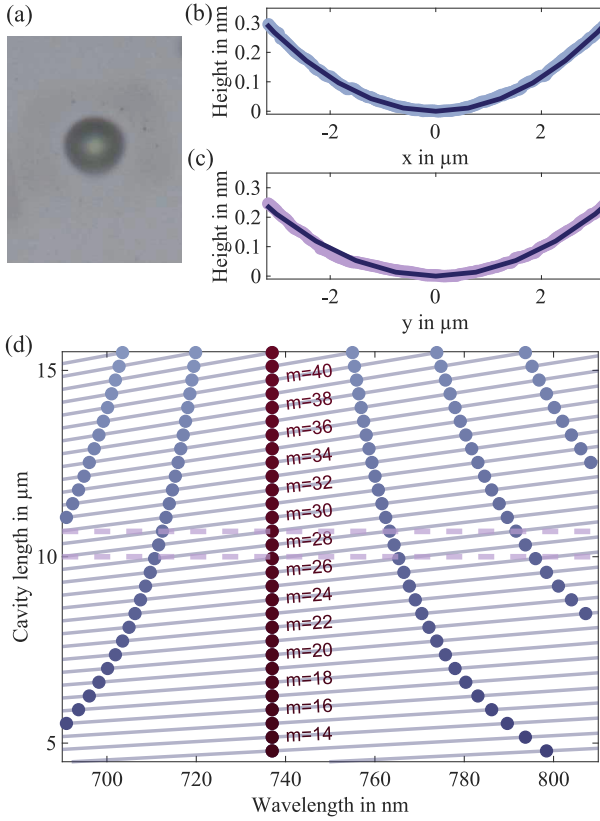


Fig. 8. Spherical structure of the hemispherical cavity and simulated mode dispersion. (a) Microscope image of the concave spherical mirror structure from CO₂-laser ablation. (b) Height profile (light blue) of the concave structure along the most curved axis reveals a RoC of 17.6 μm. (c) Height profile (purple) of the concave structure along the least curved axis reveals a RoC of 21.7 μm. (d) The simulated cavity resonance condition is shown for different cavity lengths and wavelengths (blue lines). For a cavity resonant at 737 nm (red dots), the corresponding lower and higher resonance positions (blue dots) are highlighted. The effective cavity lengths used in the measurement are indicated by the horizontal lines (purple).

Estimation on the cavity lengths are based on the position of cavity resonances in simulation Fig. 8(d). The free spectral range increases for shorter cavity lengths. Effective cavity lengths from off-resonant excitation with the ZPL resonant with $m=29$ (Fig. 4(b)) and resonant excitation with the ZPL resonant with $m=27$ (Fig. 4(d)) are highlighted.

D. Single SiV Emitter

Under resonant excitation, the membrane showed emission from single SiV⁻ color centers for longer wavelengths compared to the emitter ensemble within the implanted area. A PLE scan of a single emitter above 738.8 nm in confocal mode is shown in Fig. 9(a). At a low excitation power of 450 nW the emitter shows a nar-

row linewidth of 171.4 MHz close to the Fourier transform limit. Single emitter emission verified with a second order correlation $g^2(\tau)$ measurement in a Hanbury-Brown-Twiss configuration with 550 nW resonant laser yields a dip of $g^2(0) = 0.1$ (Fig. 9(b)). This suggests almost pure emission of one SiV⁻ color center in a resonant drive.

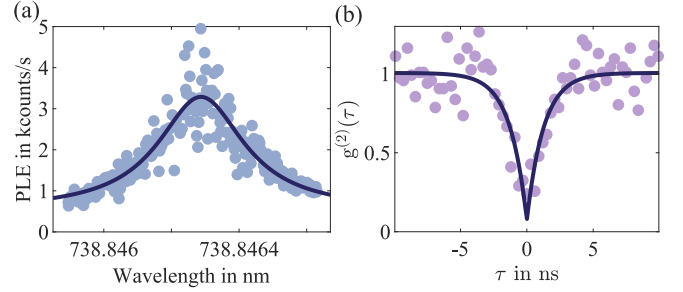


Fig. 9. Single SiV⁻ color center in a diamond membrane. (a) Photoluminescence excitation of a SiV⁻ emitter with a center wavelength of 738.8463 nm. (b) Correlation function $g^2(\tau)$ of the SiV⁻ emitter from (a) in a Hanbury-Brown-Twiss experiment. The photon antibunching suggests the emission of a single SiV⁻ emitter inside the DM.

E. Optical Lifetime

The optical lifetime of SiV⁻ emitters decreases from low temperature to RT due to other non-radiative decay channels. Free space optical lifetime measurements for SiV⁻ in diamond are summarized in Tab. II for ambient and low-temperature conditions. Two reported values are from bulk samples, one from nanowires, although the authors did not attribute any Purcell enhancement to their structures. For comparison, the measured values with off-resonant pulsing by a 700 nm diode laser (Taiko PDL M1 and DH-IB-705-B, PicoQuant GmbH) for the single-crystal of this work are shown. The values are in good agreement with the reported lifetimes.

	Bulk [42]	Bulk [2]	Nanowires [43]	DM This work
RT	1.28	1.1	1.22	1.2
70 K	-	1.54	-	1.71
4 K	1.72	1.55	1.73	1.74

Tab. II. Reported optical lifetimes for SiV⁻ in ns at different temperatures. Amongst them are lifetimes of SiV⁻ in bulk diamond: Rogers et al. [42] and Jahnke et al. [2], in nanowires: Marseglia et al. [43], and in a membrane: this work (free space).

REFERENCES

[1] M. H. Metsch, K. Senkalla, B. Tratzmiller, J. Scheuer, M. Kern, J. Achard, A. Tallaire, M. B. Plenio, P. Siyu-

shev, and F. Jelezko, Initialization and Readout of Nuclear Spins via a Negatively Charged Silicon-Vacancy Center in Diamond, *Physical Review Letters* **122**, 190503 (2019).

[2] K. D. Jahnke, A. Sipahigil, J. M. Binder, M. W. Doherty, M. Metsch, L. J. Rogers, N. B. Manson, M. D. Lukin, and F. Jelezko, Electron-phonon processes of the silicon-vacancy centre in diamond, *New Journal of Physics* **17**, 043011 (2015).

[3] T. Iwasaki, Y. Miyamoto, T. Taniguchi, P. Siyushev, M. H. Metsch, F. Jelezko, and M. Hatano, Tin-Vacancy Quantum Emitters in Diamond, *Physical Review Letters* **119**, 253601 (2017).

[4] M. Ruf, N. H. Wan, H. Choi, D. Englund, and R. Hanson, Quantum networks based on color centers in diamond, *Journal of Applied Physics* **130**, 070901 (2021).

[5] S. Meesala, Y.-I. Sohn, B. Pingault, L. Shao, H. A. Atikian, J. Holzgrafe, M. Gündoğan, C. Stavrakas, A. Sipahigil, C. Chia, R. Evans, M. J. Burek, M. Zhang, L. Wu, J. L. Pacheco, J. Abraham, E. Bielejec, M. D. Lukin, M. Atatüre, and M. Lončar, Strain engineering of the silicon-vacancy center in diamond, *Physical Review B* **97**, 205444 (2018).

[6] Y.-I. Sohn, S. Meesala, B. Pingault, H. A. Atikian, J. Holzgrafe, M. Gündoğan, C. Stavrakas, M. J. Stanley, A. Sipahigil, J. Choi, M. Zhang, J. L. Pacheco, J. Abraham, E. Bielejec, M. D. Lukin, M. Atatüre, and M. Lončar, Controlling the coherence of a diamond spin qubit through its strain environment, *Nature Communications* **9**, 2012 (2018).

[7] D. R. Assumpcao, C. Jin, M. Sutula, S. W. Ding, P. Pham, C. M. Knaut, M. K. Bhaskar, A. Panday, A. M. Day, D. Renaud, M. D. Lukin, E. Hu, B. Machielse, and M. Loncar, Deterministic creation of strained color centers in nanostructures via high-stress thin films, *Applied Physics Letters* **123**, 244001 (2023).

[8] C. T. Nguyen, D. D. Sukachev, M. K. Bhaskar, B. Machielse, D. S. Levonian, E. N. Knall, P. Stroganov, C. Chia, M. J. Burek, R. Riedinger, H. Park, M. Lončar, and M. D. Lukin, An integrated nanophotonic quantum register based on silicon-vacancy spins in diamond, *Physical Review B* **100**, 165428 (2019).

[9] X. Guo, A. M. Stramma, Z. Li, W. G. Roth, B. Huang, Y. Jin, R. A. Parker, J. Arjona Martínez, N. Shofer, C. P. Michaels, C. P. Purser, M. H. Appel, E. M. Alexeev, T. Liu, A. C. Ferrari, D. D. Awschalom, N. Delegan, B. Pingault, G. Galli, F. J. Heremans, M. Atatüre, and A. A. High, Microwave-Based Quantum Control and Coherence Protection of Tin-Vacancy Spin Qubits in a Strain-Tuned Diamond-Membrane Heterostructure, *Physical Review X* **13**, 041037 (2023).

[10] I. Karapatzakis, J. Resch, M. Schrödin, P. Fuchs, M. Kieschnick, J. Heupel, L. Kussi, C. Sürgers, C. Popov, J. Meijer, C. Becher, W. Wernsdorfer, and D. Hunger, Microwave Control of the Tin-Vacancy Spin Qubit in Diamond with a Superconducting Waveguide (2024), arxiv:2403.00521 [quant-ph].

[11] E. Janitz, M. K. Bhaskar, and L. Childress, Cavity quantum electrodynamics with color centers in diamond, *Optica* **7**, 1232 (2020).

[12] H. Kaupp, C. Deutsch, H.-C. Chang, J. Reichel, T. W. Hänsch, and D. Hunger, Scaling laws of the cavity enhancement for nitrogen-vacancy centers in diamond, *Physical Review A* **88**, 053812 (2013).

[13] R. Albrecht, A. Bommer, C. Deutsch, J. Reichel, and C. Becher, Coupling of a Single Nitrogen-Vacancy Center in Diamond to a Fiber-Based Microcavity, *Physical Review Letters* **110**, 243602 (2013).

[14] J. Benedikter, H. Kaupp, T. Hücker, Y. Liang, A. Bommer, C. Becher, A. Krueger, J. M. Smith, T. W. Hänsch, and D. Hunger, Cavity-Enhanced Single-Photon Source Based on the Silicon-Vacancy Center in Diamond, *Physical Review Applied* **7**, 024031 (2017).

[15] R. Høy Jensen, E. Janitz, Y. Fontana, Y. He, O. Gobron, I. P. Radko, M. Bhaskar, R. Evans, C. D. Rodríguez Rosenblueth, L. Childress, A. Huck, and U. Lund Andersen, Cavity-Enhanced Photon Emission from a Single Germanium-Vacancy Center in a Diamond Membrane, *Physical Review Applied* **13**, 064016 (2020).

[16] M. Ruf, M. Weaver, S. Van Dam, and R. Hanson, Resonant Excitation and Purcell Enhancement of Coherent Nitrogen-Vacancy Centers Coupled to a Fabry-Perot Microcavity, *Physical Review Applied* **15**, 024049 (2021).

[17] S. Flågan, D. Riedel, A. Javadi, T. Jakubczyk, P. Maletinsky, and R. J. Warburton, A diamond-confined open microcavity featuring a high quality-factor and a small mode-volume, *Journal of Applied Physics* **131**, 113102 (2022).

[18] F. Feuchtmayr, R. Berghaus, S. Sachero, G. Bayer, N. Lettner, R. Waltrich, P. Maier, V. Agafonov, and A. Kubanek, Enhanced spectral density of a single germanium vacancy center in a nanodiamond by cavity integration, *Applied Physics Letters* **123**, 024001 (2023).

[19] J. Heupel, M. Pallmann, J. Körber, D. Hunger, J. P. Reithmaier, and C. Popov, Fabrication of High-Quality Thin Single-Crystal Diamond Membranes with Low Surface Roughness, *physica status solidi (a)* **220**, 2200465 (2023).

[20] J. Körber, M. Pallmann, J. Heupel, R. Stöhr, E. Vasilenko, T. Hücker, L. Kohler, C. Popov, and D. Hunger, Scanning Cavity Microscopy of a Single-Crystal Diamond Membrane, *Physical Review Applied* **19**, 064057 (2023).

[21] V. Yurgens, Y. Fontana, A. Corazza, B. J. Shields, P. Maletinsky, and R. J. Warburton, Cavity-assisted resonance fluorescence from a nitrogen-vacancy center in diamond (2024), arxiv:2403.04611 [physics, physics:quant-ph].

[22] M. Salz, Y. Herrmann, A. Nadarajah, A. Stahl, M. Hettich, A. Stacey, S. Prawer, D. Hunger, and F. Schmidt-Kaler, Cryogenic platform for coupling color centers in diamond membranes to a fiber-based microcavity, *Applied Physics B* **126**, 131 (2020).

[23] G. Bayer, R. Berghaus, S. Sachero, A. B. Filipovski, L. Antoniuk, N. Lettner, R. Waltrich, M. Klotz, P. Maier, V. Agafonov, and A. Kubanek, Optical driving, spin initialization and readout of single SiV- centers in a Fabry-Perot resonator, *Communications Physics* **6**, 1 (2023).

[24] R. Zifkin, C. D. R. Rosenblueth, E. Janitz, Y. Fontana, and L. Childress, Lifetime Reduction of Single Germanium-Vacancy Defects in Diamond via a Tunable Open Microcavity (2024), arxiv:2312.14313 [quant-ph].

[25] Y. Herrmann, J. Fischer, J. M. Brevoord, C. Sauerzapf, L. G. C. Wienhoven, L. J. Feijé, M. Pasini, M. Eschen, M. Ruf, M. J. Weaver, and R. Hanson, Coherent Coupling of a Diamond Tin-Vacancy Center to a Tunable Open Microcavity (2023), arxiv:2311.08456 [quant-ph].

[26] J. Heupel, M. Pallmann, J. Körber, R. Merz, M. Kopnarski, R. Stöhr, J. P. Reithmaier, D. Hunger, and C. Popov, Fabrication and Characterization of Single-Crystal Diamond Membranes for Quantum Photonics with Tunable Microcavities, *Micromachines* **11**, 1080 (2020).

[27] J. Lang, S. Häußler, J. Fuhrmann, R. Waltrich, S. Ladadha, J. Scharpf, A. Kubanek, B. Naydenov, and F. Jelezko, Long optical coherence times of shallow-implanted, negatively charged silicon vacancy centers in diamond, *Applied Physics Letters* **116**, 064001 (2020).

[28] M. Challier, S. Sonusen, A. Barfuss, D. Rohner, D. Riedel, J. Koelbl, M. Ganzhorn, P. Appel, P. Maletinsky, and E. Neu, Advanced Fabrication of Single-Crystal Diamond Membranes for Quantum Technologies, *Micromachines* **9**, 148 (2018).

[29] E. I. Rosenthal, C. P. Anderson, H. C. Kleidermacher, A. J. Stein, H. Lee, J. Grzesik, G. Suri, A. E. Rugar, D. Riedel, S. Aghaeimeibodi, G. H. Ahn, K. Van Gasse, and J. Vučković, Microwave Spin Control of a Tin-Vacancy Qubit in Diamond, *Physical Review X* **13**, 031022 (2023).

[30] G. Pieplow, M. Belhassen, and T. Schröder, Efficient microwave spin control of negatively charged group-IV color centers in diamond, *Physical Review B* **109**, 115409 (2024).

[31] S. Vadia, J. Scherzer, H. Thierschmann, C. Schäfermeier, C. Dal Savio, T. Taniguchi, K. Watanabe, D. Hunger, K. Karraï, and A. Högele, Open-Cavity in Closed-Cycle Cryostat as a Quantum Optics Platform, *PRX Quantum* **2**, 040318 (2021).

[32] S. Häußler, G. Bayer, R. Waltrich, N. Mendelson, C. Li, D. Hunger, I. Aharonovich, and A. Kubanek, Tunable Fiber-Cavity Enhanced Photon Emission from Defect Centers in hBN, *Advanced Optical Materials* **9**, 2002218 (2021).

[33] D. Hunger, T. Steinmetz, Y. Colombe, C. Deutsch, T. W. Hänsch, and J. Reichel, A fiber Fabry-Perot cavity with high finesse, *New Journal of Physics* **12**, 065038 (2010).

[34] T. Ruelle, D. Jaeger, F. Fogliano, F. Braakman, and M. Poggio, A tunable fiber Fabry-Perot cavity for hybrid optomechanics stabilized at 4 K, *Review of Scientific Instruments* **93**, 095003 (2022).

[35] N. Tomm, A. Javadi, N. O. Antoniadis, D. Najar, M. C. Löbl, A. R. Korsch, R. Schott, S. R. Valentini, A. D. Wieck, A. Ludwig, and R. J. Warburton, A bright and fast source of coherent single photons, *Nature Nanotechnology* **16**, 399 (2021).

[36] S. B. van Dam, M. Ruf, and R. Hanson, Optimal design of diamond-air microcavities for quantum networks using an analytical approach, *New Journal of Physics* **20**, 115004 (2018).

[37] C. T. Nguyen, D. D. Sukachev, M. K. Bhaskar, B. Machielse, D. S. Levonian, E. N. Knall, P. Stroganov, R. Riedinger, H. Park, M. Lončar, and M. D. Lukin, Quantum Network Nodes Based on Diamond Qubits with an Efficient Nanophotonic Interface, *Physical Review Letters* **123**, 183602 (2019).

[38] M. K. Bhaskar, R. Riedinger, B. Machielse, D. S. Levonian, C. T. Nguyen, E. N. Knall, H. Park, D. Englund, M. Lončar, D. D. Sukachev, and M. D. Lukin, Experimental demonstration of memory-enhanced quantum communication, *Nature* **580**, 60 (2020).

[39] P.-J. Stas, Y. Q. Huan, B. Machielse, E. N. Knall, A. Suleymanzade, B. Pingault, M. Sutula, S. W. Ding, C. M. Knaut, D. R. Assumpcao, Y.-C. Wei, M. K. Bhaskar, R. Riedinger, D. D. Sukachev, H. Park, M. Lončar, D. S. Levonian, and M. D. Lukin, Robust multi-qubit quantum network node with integrated error detection, *Science* **378**, 557 (2022).

[40] S. Häußler, J. Benedikter, K. Bray, B. Regan, A. Dietrich, J. Twamley, I. Aharonovich, D. Hunger, and A. Kubanek, Diamond photonics platform based on silicon vacancy centers in a single-crystal diamond membrane and a fiber cavity, *Physical Review B* **99**, 165310 (2019).

[41] E. Neu, M. Agio, and C. Becher, Photophysics of single silicon vacancy centers in diamond: Implications for single photon emission, *Optics Express* **20**, 19956 (2012).

[42] L. J. Rogers, K. D. Jahnke, T. Teraji, L. Marseglia, C. Müller, B. Naydenov, H. Schauffert, C. Kranz, J. Isoya, L. P. McGuinness, and F. Jelezko, Multiple intrinsically identical single-photon emitters in the solid state, *Nature Communications* **5**, 4739 (2014).

[43] L. Marseglia, K. Saha, A. Ajoy, T. Schröder, D. Englund, F. Jelezko, R. Walsworth, J. L. Pacheco, D. L. Perry, E. S. Bielejec, and P. Cappellaro, Bright nanowire single photon source based on SiV centers in diamond, *Optics Express* **26**, 80 (2018).

[44] J. M. Binder, A. Stark, N. Tomek, J. Scheuer, F. Frank, K. D. Jahnke, C. Müller, S. Schmitt, M. H. Metsch, T. Unden, T. Gehring, A. Huck, U. L. Andersen, L. J. Rogers, and F. Jelezko, Qudi: A modular python suite for experiment control and data processing, *SoftwareX* **6**, 85 (2017).

[45] T. Lühmann, R. John, R. Wunderlich, J. Meijer, and S. Pezzagna, Coulomb-driven single defect engineering for scalable qubits and spin sensors in diamond, *Nature Communications* **10**, 4956 (2019).

[46] S. Tamura, G. Koike, A. Komatsubara, T. Teraji, S. Onoda, L. P. McGuinness, L. Rogers, B. Naydenov, E. Wu, L. Yan, F. Jelezko, T. Ohshima, J. Isoya, T. Shinada, and T. Tanii, Array of bright silicon-vacancy centers in diamond fabricated by low-energy focused ion beam implantation, *Applied Physics Express* **7**, 115201 (2014).

[47] T. Schröder, M. E. Trusheim, M. Walsh, L. Li, J. Zheng, M. Schukraft, A. Sipahigil, R. E. Evans, D. D. Sukachev, C. T. Nguyen, J. L. Pacheco, R. M. Camacho, E. S. Bielejec, M. D. Lukin, and D. Englund, Scalable focused ion beam creation of nearly lifetime-limited single quantum emitters in diamond nanostructures, *Nature Communications* **8**, 15376 (2017).

[48] S. Lagomarsino, A. M. Flatae, S. Sciortino, F. Gorelli, M. Santoro, F. Tantussi, F. De Angelis, N. Gelli, F. Tacchetti, L. Giuntini, and M. Agio, Optical properties of silicon-vacancy color centers in diamond created by ion implantation and post-annealing, *Diamond and Related Materials* **84**, 196 (2018).

[49] J. A. Zuber, M. Li, M. Grima Puigibert, J. Happacher, P. Reiser, B. J. Shields, and P. Maletinsky, Shallow Silicon Vacancy Centers with Lifetime-Limited Optical Linewidths in Diamond Nanostructures, *Nano Letters* **23**, 10901 (2023).